Mechanisms for Microparticle Dispersion in a Jet in Crossflow

Marina Campolo
Instituto Pluridisciplinar, Universidad Complutense de Madrid, 28040 Madrid, Spain

and

Centro Interdipartimentale di Fluidodinamicae Idraulica, Università di Udine, 33100 Udine, Italy

Maria Vittoria Salvetti
Dipartimento di Ingegneria Aerospaziale, Università di Pisa, 56122 Pisa, Italy

Alfredo Soldati
Centro Interdipartimentale di Fluidodinamica e Idraulica and Dipartimento di Energetica e Macchine, Università di Udine, 33100 Udine, Italy

DOI 10.1002/aic.10301
Published online in Wiley InterScience (www.interscience.wiley.com).

The dispersion produced by a jet injecting microparticles in a cross stream is controlled by the interaction between dispersed species and large-scale time-dependent flow structures populating the transverse jet. These structures span over a wide range of spatial and temporal scales and are not equally effective in advecting and dispersing species. In many environmental and industrial applications, the species advected by the jet stream are expected to undergo rapid and homogeneous dilution away from the injection point. Preferential accumulation of particles into specific flow regions may have consequences on the overall industrial process. For instance, nonuniform particle distribution can severely downgrade the efficiency of postcombustion devices. In this work, we address the problem of identifying which of the flow structures in a jet in crossflow controls dispersion mechanisms of inertial particles, focusing specifically on the issue of their preferential distribution. The flow field produced by the transverse jet is calculated using a finite-volume solver of Navier–Stokes equations and the dispersion of particles is computed using a Lagrangian approach. We investigate the behavior of particles of different sizes, examining 5 orders of magnitude of their inertial parameter—the particle timescale. The analysis of dispersion shows that particle distribution is not uniform and is dominated by specific flow structures. Examining the distribution of the different particles in connection with particle timescale and flow structure evolution, it is found that shear layer vortices initially control dispersion and segregation processes, whereas counter-rotating vortices entrain and trap particles in the lee side of the jet. *AIChE J,* 51: 28–43, 2005
Keywords: transverse jet, dispersion, segregation, combustion, microparticles

Introduction

Transverse jets are used in many engineering and environmental applications for efficient dispersion of the species—particles or droplets—injected in the main transverse stream. Fuel injection in combustion chambers, postcombustion control devices (such as transverse injection of ammonia solution for NO_x abatement), hot gas quenching with sprays, and spray dryers are but a few examples of these flow configurations in engineering applications. In all of these applications, the extent and homogeneity of dispersion provide crucial information to size and optimize devices and processes. The extent of disper-

Correspondence concerning this article should be addressed to A. Soldati at soldati@uniud.it.

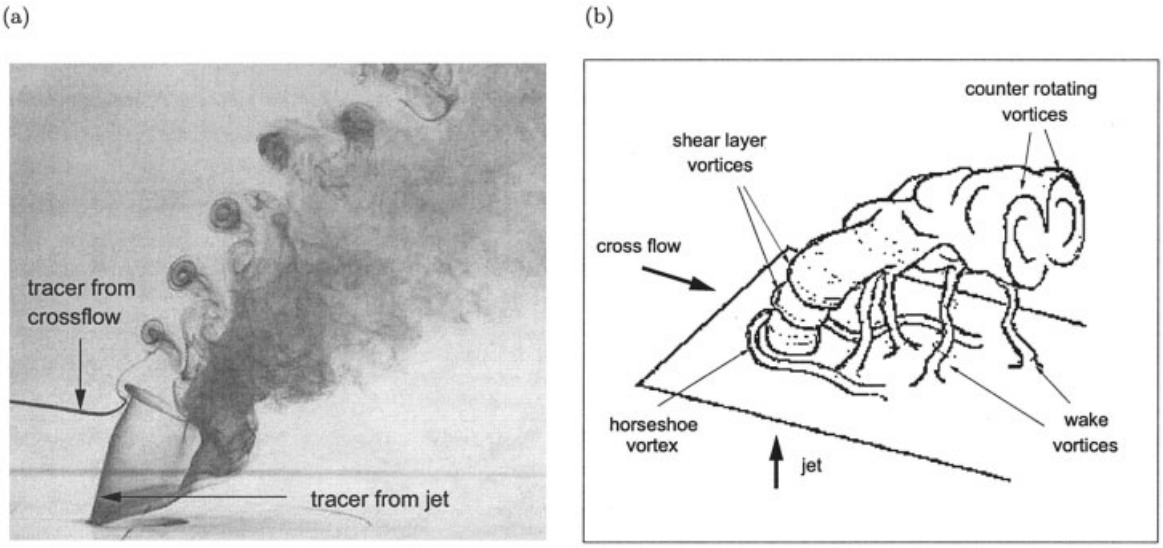

Figure 1. Vortical structures characteristic of transverse jet.

(a) Roll-up of shear layer vortices (reprint from Kelso et al.[10]); (b) vortical structures in near-field of transverse jet (reprint from Fric and Roshko[9]).

sion is related to jet penetration into the crossflow and has been investigated by Cleaver and Edwards[1] and by Gosh and Hunt,[2] among others. The homogeneity of the dispersion is an open topic of research and is currently a critical issue in many applications that also involve chemical reactions because, if reaction rates depend on the local and instantaneous concentration of dispersed species, there is experimental evidence[3] that the instantaneous concentration field may be significantly different from the time-averaged field. Instantaneous concentration fluctuations are generated by the interaction between particles and structures in the flow field and the nonhomogeneous distribution of dispersed species has detrimental effects that depend on the specific application. As an example, in combustion devices fuel-rich combustion leads to high local temperatures and pollutant formation; in safety release systems, the nonhomogeneous dispersion of flammable material increases the distance over which ignition may occur. These effects can be controlled only by careful optimization of devices and processes from the design stage on. However, sizing of devices and process optimization are still based on statistical Fickian diffusion models,[4] which can treat particle dispersion only in a time-averaged sense. These models cannot predict the highly nonuniform distribution of phases, and do not reproduce the true physics of the dispersion process. Different (time-dependent, Lagrangian type) approaches are required for a deeper understanding of the mechanisms for particle dispersion and preferential concentration. In transverse jets, the precise analysis of particle and flow structure dynamics is complicated by the strongly time dependent nature of the dispersion process and by the number of the different flow scales mutually interacting, which are not equally effective in advecting and dispersing particles.[5] In particular, specific attention must be paid to the structures larger than the smallest, more homogeneous, turbulent scales. These larger structures have sufficient spatial and temporal coherence to control the motion of inertial particles in a variety of turbulent flows, from homogeneous turbulence,[6] to boundary layer turbulence,[7] and to turbulent jets.[8]

The fluid dynamics of transverse jets has been extensively investigated by experiments (see, for instance, Fric and Roshko[9] and Kelso et al.[10]) and numerical simulations,[11,12] which helped to identify the main characteristic large-scale structures, and their generation process.[10] It will be useful for future discussion to describe these structures and we will use the insightful images originally published by Fric and Roshko[9] and by Kelso et al.[10] In Figure 1a (from Kelso et al.[10]), the generation of the regular array of shear layer vortices is demonstrated by the behavior of the smoke tracers coming from the jet and from the crossflow, which merge together. The shear layer vortices are generated originally as ring vortices. Their upper part moves downstream in a regular way, whereas their lee side portion bends upward (see Kelso et al.[10] and Cortelezzi and Karagozian[13]) and contributes to the formation of the counterrotating vortices, responsible for crossflow entrainment into the jet core (see Figure 13 in Cortelezzi and Karagozian[13]). Counterrotating vortices are shown in Figure 1b (from Fric and Roshko[9]) together with the wake vortices. Horseshoe vortices are also shown, even if there is not clear consensus whether they are real structures or fossils of the flow visualization techniques that have been used to detect them (for a discussion see Morton and Ibbetson[14]). All these flow structures interact in a complex way, and their dynamics has been investigated by Kelso et al.[10,15] and by Cortelezzi and Karagozian,[13] among others. Because our objective is to examine particle distribution in such a complicated flow field, we must examine particle dynamics in connection with the dynamics of these flow structures.

Particle dispersion was studied in axisymmetric jets by Chung and Troutt[16] and by Anderson and Longmire,[17] among others, in coaxial jets by Apte et al.,[18] and in-plane mixing layers by Chein and Chung,[19] Crowe et al.,[20] Wen et al.,[21] Marcu and Meiburg,[22] and Yang et al.,[23] among others. These studies have shown that the large-scale flow structures, which form in the shear layers, play a major role in the advection processes because they generate directed (nonrandom) motion

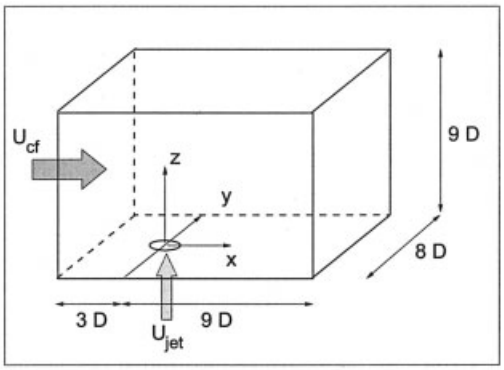

Figure 2. Geometry of computational domain considered and reference coordinate system, centered at jet exit.

of particles leading to preferential concentration. The underlying idea driving most of these investigations, and also this work, is that understanding the relationships between fluid dynamics and particle preferential distribution may provide a tool to control instantaneous particle concentration field (Karagozian et al.[24] and references therein).

In particle-laden flows, the key parameter controlling dispersion is the Stokes number (St), which is the ratio between the particle aerodynamic response time and the relevant flow timescale. In particular, previous studies[20] remark that the strongest interaction (such as interactions leading to preferential distribution) is found for particles and structures having similar timescales (that is, for $St \simeq 1$).

A review of the literature underlines that extensive studies on particle dispersion in the transverse jet configuration are still lacking. In particular, Han and Chung[25] developed an integral model to predict the average behavior of a two-phase gas-particle transverse jet. Gosh and Hunt[2] investigated the dynamics of spray jets in a crossflow, developing analytical models to calculate the spray drift for different values of the jet-to-crossflow velocity ratio. Yi and Plesniak[26] investigated experimentally the dispersion of particles into a confined rectangular crossflow, finding that particle distribution depends on particle shape and size. Remarkably, we did not find a study in which dispersion of inertial particles was examined in connection with the time-dependent dynamics of the flow structures of the transverse jet. In this work, we will use a finite-volume solver of Navier–Stokes equations to simulate the flow field of the transverse jet and Lagrangian tracking to investigate the dispersion mechanisms of microparticles. The purposes of this paper are thus (1) to characterize the behavior of inertial particles of different size (and response time) in the transverse jet, (2) to identify the mechanisms that lead to possible preferential distribution of particles, and (3) to evaluate the effect of the interaction between particle dynamics and fluid dynamics, to identify the scales controlling dispersion.

Methodology

Computational domain and numerical simulation

Figure 2 shows the computational domain for the jet in crossflow: the fluid is air ($\nu = 1.29 \times 10^{-5}$ m^2/s, $\rho = 1.4$ kg/m^3), the crossflow enters the box from left to right (unperturbed velocity $U_{cf} = 0.514$ m/s), and the jet is issued orthogonally from the orifice in the lower wall (jet exit centerline velocity $U_{jet} = 2.57$ m/s). The reference coordinate system is centered at the jet-exit, with x, y, and z representing streamwise, spanwise, and vertical directions, respectively. All quantities are made dimensionless using the jet orifice diameter ($D = 0.01$ m) as a reference length scale, the jet exit centerline velocity U_{jet} as a reference velocity, and the reference time $t_u = D/U_{jet} = 3.89 \times 10^{-3}$ s. We use the superscript $+$ to indicate dimensionless values. In dimensionless coordinates, the domain is $12 \times 8 \times 9$ in the streamwise, spanwise, and vertical directions, respectively. The jet exit is $3D$ downstream from the crossflow inlet.

Conditions examined correspond to $\mathrm{Re}_{jet} = U_{jet}D/\nu = 2000$, $\mathrm{Re}_{cf} = U_{cf}D/\nu = 400$, and to a jet-to-crossflow velocity ratio $R = U_{jet}/U_{cf} = 5$. These conditions ensure the formation of several types of large-scale structures[10] and have been also investigated by Rudman,[27] who solved the Navier–Stokes equations using a code based on the piecewise parabolic method of Collela and Woodward[28] in combination with the linearized Riemann solver of Roe.[29]

Throughout this study, we use the finite-volume solver previously described by Zang et al.[30] For the purpose of numerical validation, we use the same assumptions and the same grid resolution adopted by Rudman.[27] Specifically, boundary conditions are: (1) laminar, boundary layer velocity profile of the crossflow at the inlet (thickness $\delta^+ = 0.5$); (2) analytical, axisymmetric velocity profile at the pipe outlet (boundary layer thickness in the pipe $\theta^+ = 0.03$), given by

$$U^+(r^+) = \frac{1}{2}\left\{1 - \tanh\left[\frac{1}{8\theta^+}\left(2r^+ - \frac{1}{2r^+}\right)\right]\right\} \qquad (1)$$

(3) free-slip boundary condition at the upper x–y plane and at the box sides (see Figure 2); (4) zero gradient outflow condition at the box outlet; and (5) no-slip condition at the lower wall.

The grid is uniform and made of 84 x 56 x 44 finite volumes, corresponding to a grid resolution Δx, Δy, and Δz equal to 4.67, 4.67, and 6.81 times the shear layer thickness at the jet exit, which is the relevant length scale for the mixing layer. This resolution is sufficient to capture the evolution of the larger vortices as shown in Figure 1. A posteriori analyses have shown that the cross section of the smaller shear layer vortex is described by at least nine grid points. A simulation of the same flow conditions performed with a grid twice as refined in each direction for a time period of 50 time units has shown no significant difference (<5% difference in the calculation of the local flow field).

The grid previously described has been used to calculate the field evolution, starting from the condition of still fluid for the time period necessary to achieve statistical convergence (about 3 times the throughflow period, corresponding to 200 time units). Then, we calculated the flow field evolution for a time period of 450 time units (about 6.6 times the throughflow period). This period was larger than needed for the calculation of particle dispersion and yet was required to have sufficient data to compute flow field statistics.

Finite-volume solver

For the incompressible flow considered here, the governing equations are Navier–Stokes and continuity equations (omitted here for sake of brevity; the reader is referred to the article by Zang et al.[30]). Governing equations are discretized on a colocated grid using a finite-volume approach, following the technique proposed in Zang and Street.[31]

The solver uses two sets of variables, defining Cartesian velocities and pressure at cell centers, and contravariant volume fluxes at the cell faces. A fractional step method is used to advance in time, and pressure is obtained by solving a Poisson equation with a multigrid algorithm. Time marching is semi-implicit; the global formal accuracy is second order both in space and time. Details of the numerical method, extensive validation, and application to different types of flows can be found in Zang et al.[30] and Zang and Street.[31]

We should remark here that the present simulation is not a direct numerical simulation (DNS) because we do not solve all turbulence scales down to the viscous dissipation. Currently, there is not a single DNS of this flow configuration, which is probably out of reach for the most powerful computational center.[11] Our simulation is not a large-eddy simulation either because we do not use any subgrid scale (SGS) model. Our object in this work is to investigate the dynamics of the large-scale structures that form at the jet exit where the shear layer separates. These structures are geometry dependent and dominate particle distribution in the near field of the jet. According to Yule,[32] these structures are transitional (that is, *not yet turbulent* structures), clearly identifiable as large-scale motions as shown in Figure 1. Only further downstream, these large-scale structures interact strongly with the higher-frequency scales of the turbulence, losing coherence and forming noncoherent, turbulent vorticity regions.

We did check that the grid resolution gives a reliable prediction of the dynamics of large scales, in which we are interested, without the need of an SGS model. Moreover, although our resolution is coarse for a DNS, it is not so coarse as to have serious problems of lack of dissipation and thus of numerical instabilities. Because the numerical scheme is only second order, it provides damping of the highest resolved frequencies (see Lele[33]).

Lagrangian tracking

Once we obtained a fully developed flow, we simulated the behavior of 2×10^4 water droplets (density $\rho_p = 1000\ \mathrm{kg/m^3}$). Here, we use the words *droplets* and *particles* interchangeably to indicate the dispersed phase. We should remark here that observations made for *particle* behavior may be extended to *droplet* behavior in case of dilute flow approximation when the effects attributed to particle–particle interaction and wall–particle interaction can be neglected.

As observed by Kelso et al.[10] and by Yuan et al.,[11] the jet in crossflow is characterized by flow structures of different sizes and timescales (see Figure 1). We expect that particles of different diameters will interact selectively with these vortices, depending on their Stokes number. We chose to simulate particle diameters from 1 to 200 μm, for which the dimensionless characteristic time, $\tau_p^+ = \rho_p D_p^2/18\mu t_u$, varies from 7.92×10^{-4} to 3.16×10^1 time units. Details of particle simulations are reported in Table 1.

Table 1. Characteristics of Simulated Particles: Dimensional and Dimensionless Particle Diameter, D_p and D_p^+, and Response Time, τ_p and τ_p^+ *

D_p (μm)	D_p^+	τ_p (s)	τ_p^+
1	1.0×10^{-4}	3.08×10^{-6}	7.92×10^{-4}
10	1.0×10^{-3}	3.08×10^{-4}	7.92×10^{-2}
100	1.0×10^{-2}	3.08×10^{-2}	7.92×10^{0}
150	1.5×10^{-2}	6.92×10^{-2}	2.47×10^{1}
200	2.0×10^{-2}	1.23×10^{-1}	3.16×10^{1}

*Reference length scale is jet orifice diameter ($D = 0.01$ m), reference velocity is jet exit centerline velocity U_{jet}, and reference time is $t_u = D/U_{jet}$.

We calculate the trajectory of each particle by integrating explicitly over time the equation of motion. The assumptions for particle modeling are: (1) all particles are noninteracting, nondeformable solid spheres; (2) particle density is large compared to fluid density; (3) the effect of the particles on the flow is neglected; and (4) virtual mass, pressure gradient, and Basset forces are neglected. According to many previous reports (see, for instance, Chung and Troutt[16] and Loth[34]), the study of the order of magnitude of the forces acting on particles based on the equation of motion derived by Maxey and Riley[35] reveals that the drag force is $O(\mathrm{St}^{-1})$, the virtual mass and the pressure gradient are $O[(\rho/\rho_p)^1]$ and the Basset force is $O[(\rho/\rho_p)^{1/2}]$, where ρ and ρ_p are fluid density and particle density, respectively. In our work, $\rho/\rho_\mathrm{p} \simeq O(10^{-3})$ and St based on the reference timescale for the fluid, reported as τ_p^+ in Table 1, is in the range $[10^{-4} \div 10^1]$. Therefore, for the specific flow systems examined here, neglected terms have a limited effect, and the equation of motion reduces to a balance of Stokes drag, buoyancy forces, and particle inertia.

The equation of particle motion can be written as

$$\rho_p \frac{\pi D_p^3}{6} \frac{d\mathbf{v}_p}{dt} = \frac{1}{2} C_D \frac{\pi D_p^2}{4} \rho(\mathbf{v} - \mathbf{v}_p)|\mathbf{v} - \mathbf{v}_p| + \frac{\pi D_p^3}{6}(\rho_p - \rho)\mathbf{g} \tag{2}$$

where D_p and $\mathbf{v}_p$ are particle diameter and velocity, respectively; $\mathbf{v}$ is fluid velocity; t is time; $\mathbf{g}$ is gravity; and $C_D = f(\mathrm{Re}_p)$ is the Stokes coefficient for drag, where $\mathrm{Re}_p = \rho D_p \lceil \mathbf{v} - \mathbf{v}_p \rceil / \mu$ is the particle Reynolds number.

The drag force is evaluated by calculating the fluid velocity $\mathbf{v}$ at each particle position using trilinear interpolation of velocity values at cell centers. We use the Stokes coefficient for drag, with the following nonlinear correction, when $\mathrm{Re}_p > 1$,[36] expressed as

$$C_D(\mathrm{Re}_p) = \frac{24}{\mathrm{Re}_p}(1 + 0.15\,\mathrm{Re}_p^{0.687}) \tag{3}$$

Particles are released at the jet exit. Specifically, 10^4 particles, referred to as *inner particles*, are uniformly distributed in the inner circle $r^+ \le D^+/2 - \theta^+ = 0.47$, where θ^+ is the boundary layer thickness in the pipe, whereas 10^4 particles, referred to as *outer particles*, are uniformly distributed in the outer ring $0.47 < r^+ < 0.5$. We decided to distribute particles in this nonuniform way because Lagrangian particle tracking is time consuming and, to obtain more accurate statistics, we

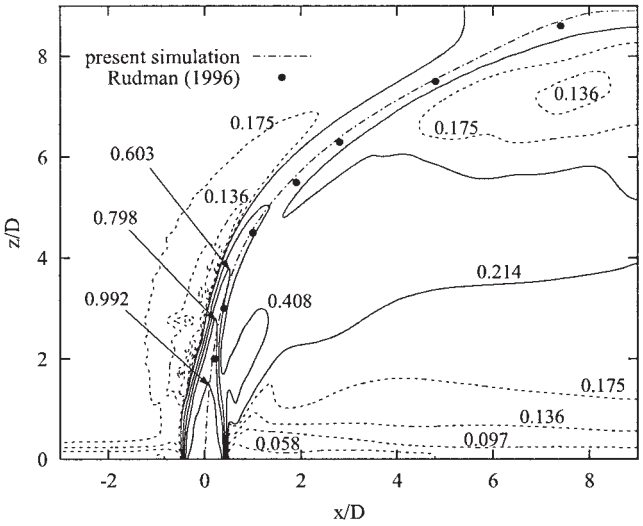

Figure 3. Time-averaged modulus of velocity field in jet symmetry plane (dimensionless value).

Solid lines are $U^+ > U^+_{cf} = 0.2$ and dashed lines are $U^+ < U^+_{cf}$. Comparison between jet axis calculated by Rudman[27] (symbols) and present simulation (dash dot line).

planned to have a larger number of particles in the region where the flow structures form. Particle initial velocity is set equal to the local fluid velocity. Equation 2 is integrated with an explicit Runge–Kutta fourth-order method and the integration time step for all particles is one tenth of the characteristic time of the smallest particle, $\tau_p^{1\mu m}$.

Results

Qualitative structure of the flow field

Figure 3 shows isocontours of the calculated, time-averaged modulus of the velocity field in the jet symmetry plane. Solid lines and dashed lines identify dimensionless velocity values, respectively, larger and lower than crossflow velocity ($U^+_{cf} = 0.2$). As expected in this flow configuration, the crossflow bends the high velocity tip of the jet and the jet velocity profile is rapidly blunted by this interaction. Isocontours shown in Figure 3 are in qualitative agreement with the results of the accurate large-eddy simulation of Yuan et al.,[11] even though we could not make quantitative comparison because we computed different flow conditions ($\mathrm{Re}_{cf} = 400$ and $R = 5$ against $\mathrm{Re}_{cf} = 1050$ and 2100, and $R = 3.3$ and 4). The calculated jet axis—defined as the locus of the points of maximum velocity—is in agreement with data reported by Rudman,[27] shown as solid dots on the graph. The small differences observed in the position of the jet axis may possibly be attributable to the different numerical approaches.

For the purpose of the work, it is important to describe the dynamics of the flow structures because these will dominate particle transport. We will describe here briefly the main structures of the flow field, addressing the reader to previous papers for a more comprehensive analysis.[9,10] All the vortical structures characteristic of the jet in crossflow are produced in the jet-exit region. As shown in Figure 1b, shear layer vortices dominate the initial portion of the jet, and wake vortices form on the downstream side of the jet. Farther downstream, the pair of streamwise counterrotating vortices dominates the flow field: as discussed in many previous works,[10,13] these structures, averaged over time, produce the counterrotating vortex pair (CVP). Jet shear layer vortices and wake vortices are unsteady and experiments have shown that wake vortices are shed at characteristic Strouhal frequencies.[9]

As in Kelso et al.,[10] we visualize the structures of the flow field using snapshots of vorticity. In Figure 4 we show snapshots taken every 0.02 s (5.14 time units) from $t = 1.06$ s to $t = 1.1$ s. This time window includes three realizations of the periodic roll-up of shear layer vortices and is sufficient to visualize many of the characteristic features of the flow field. Figures 4a–4c show isocontours of spanwise vorticity (ω_y^+) in the symmetry plane: from these isocontours, shear layer vortices can be identified and followed in their dynamics. Figures 4d–f show isocontours of streamwise vorticity (ω_x^+) in the front view (y–z) plane located at $x^+ = 8.5$, downstream from the jet exit: from these isocontours the counterrotating vortices can be identified and examined. Consider first Figures 4a–4c, in which dimensionless isocontour values are -0.390, -0.195, 0.195, and 0.390. Solid lines characterize isocontours of negative vorticity (that is, clockwise rotation) and dashed lines characterize isocontours of positive vorticity (that is, counterclockwise rotation). From the snapshots sequence, we observe that pairs of positive and negative closed contours of spanwise vorticity (that is, vorticity rings),[10] indicated as A, a and B, b in Figure 4, form quasi-periodically from the upper and lower sides of the jet. We should remark here that only a subset of the closed, spanwise vorticity isocontours shown in Figure 4 can be identified as shear layer vortices. These structures, characterized by positive vorticity in the upper side of the jet and negative vorticity in the lower side of the jet, are the primary signature of a Kelvin–Helmoltz type instability and show strong spatial and temporal coherence. They should not be confused with blotches of negative vorticity found in the upper side of the jet and positive vorticity found in the lower side of the jet, respectively (see structures labeled Z, z in Figure 4). These are secondary structures generated in between subsequent ring vortices and characterized by weak spatial and temporal coherence.[10]

Consider now Figures 4d–4f, in which dimensionless isocontour values are -0.390, -0.195, -0.097, 0.097, 0.195, and 0.390. Solid lines characterize isocontours of positive vorticity (that is, counterclockwise rotation) and dashed lines characterize isocontours of negative vorticity (that is, clockwise rotation). The main structures of the transverse jet visible in the figure are the counterrotating vortices. The instantaneous structures are nonsteady and nonsymmetric[3,37,38] and very complex in shape. Specifically, the structure on the left side is characterized by an external layer of positive vorticity, whereas the structure on the right side is characterized by an external layer of negative vorticity. Regions of opposite signed vorticity superimpose to these structures in the core of the curved jet. According to Yuan et al.,[11] the breaking of spanwise rollers may be responsible for the generation of this very intense vortical field characterized by streamwise vorticity values one order of magnitude larger than the background vorticity of counterrotating vortices. The action of the instantaneous structures is to entrain fluid from the crossflow into the body of the jet, generating strong mixing. This fluid entrainment shows also from the time average of the flow field (see Figure 13 in

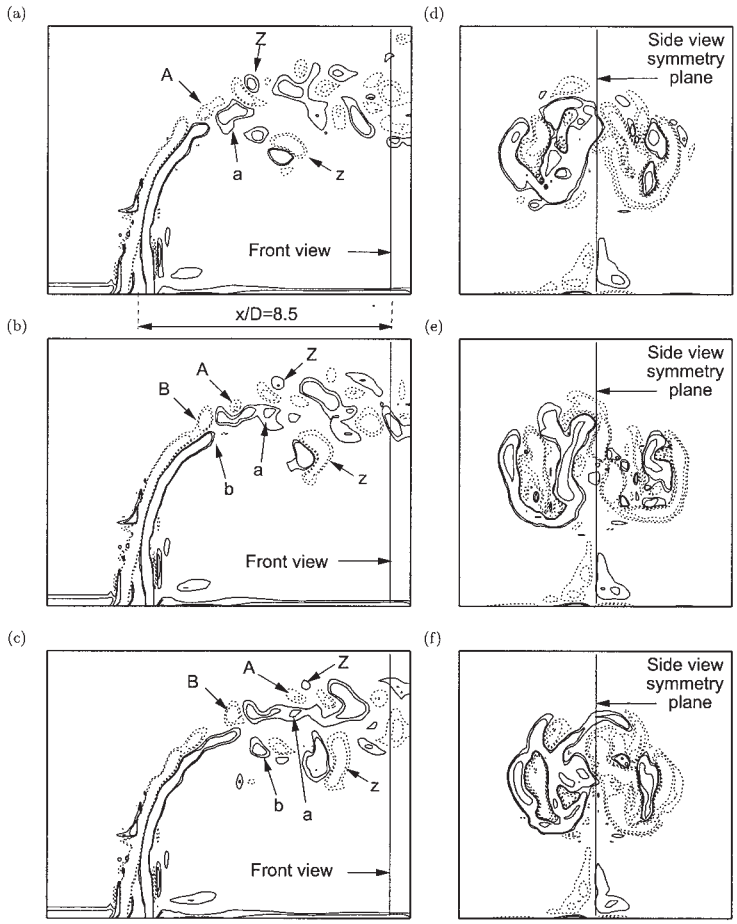

Figure 4. Time evolution of flow structures.

Roll-up of shear layer vortices (left), identified by isocontours of spanwise vorticity, and oscillation of counterrotating vortices (right), identified by isocontours of streamwise vorticity. Isocontours (dimensionless) are −0.390, −0.195 (solid lines, clockwise rotation) and 0.195, 0.390 (dashed lines, counterclockwise rotation) for spanwise vorticity, and −0.390, −0.195, −0.097 (dashed lines, clockwise rotation) and 0.097, 0.195, and 0.390 (solid lines, counterclockwise rotation) for streamwise vorticity.

Cortelezzi and Karagozian[13]). The two smaller patches of vorticity of opposite sign near to the bottom wall identify the cornerlike regions in which opposite circulation is induced by the counterrotating vortices.

From a qualitative perspective, the structures discussed here and their dynamics confirm previous experimental[10] and numerical[11] works.

Formation frequency of large-scale structures

The flow structures briefly examined are time-dependent. Specifically, different timescales characterize the different flow structures and their generation dynamics, and a periodic behavior has been observed for wake vortex shedding and for the time generation of the shear layer vortices. To characterize shear layer vortices and wake vortices, we measure the characteristic advection timescale of both structures. We sample the vorticity in the points shown in Figure 5a. The first array of sensors (A, B, and C) is in the region of the flow near the jet axis, where shear layer roll-up is expected. As an example, a 0.35-s (90 time units) window of the time series of spanwise vorticity, ω_y^+, is shown in Figure 5b. Periodic oscillations of ω_y^+ are found at the three sensor locations, yet the amplitude of the signal is significantly different. At sensor A, the signal is characterized by small fluctuations and we observe a larger variation of ω_y^+ only at $t \simeq 0.8$ s and at $t \simeq 0.96$ s for a small time period. At sensor B, fluctuations have larger amplitude, and the localized increase in amplitude at $t \simeq 0.8$ s and at $t \simeq 0.96$ s is again observed. At sensor C, fluctuations in amplitude become even larger and the signal appears as a frequency-modulated wave.

The second array of sensors (a, b, and c) is placed near the lower wall and downstream from the jet exit to find the footprint of wake vortices. A time-series window of the wall normal vorticity, ω_z^+, is shown in Figure 5c. Periodic fluctuations are characterized by frequencies lower than those in Figure 5b, indicating that shear layer vortices and wake vortices are generated by different instabilities. At sensor b, which is in the symmetry plane, fluctuations average to zero, whereas at sensors a and c average values of ω_z^+ are negative (counterclockwise rotation) and positive (clockwise rotation), respectively.

The oscillation period $T_{roll\text{-}up}$ of ω_y^+ is the time between generation of subsequent shear layer vortices, whereas the oscillation period T_{wake} of ω_z^+ is the time between generation of

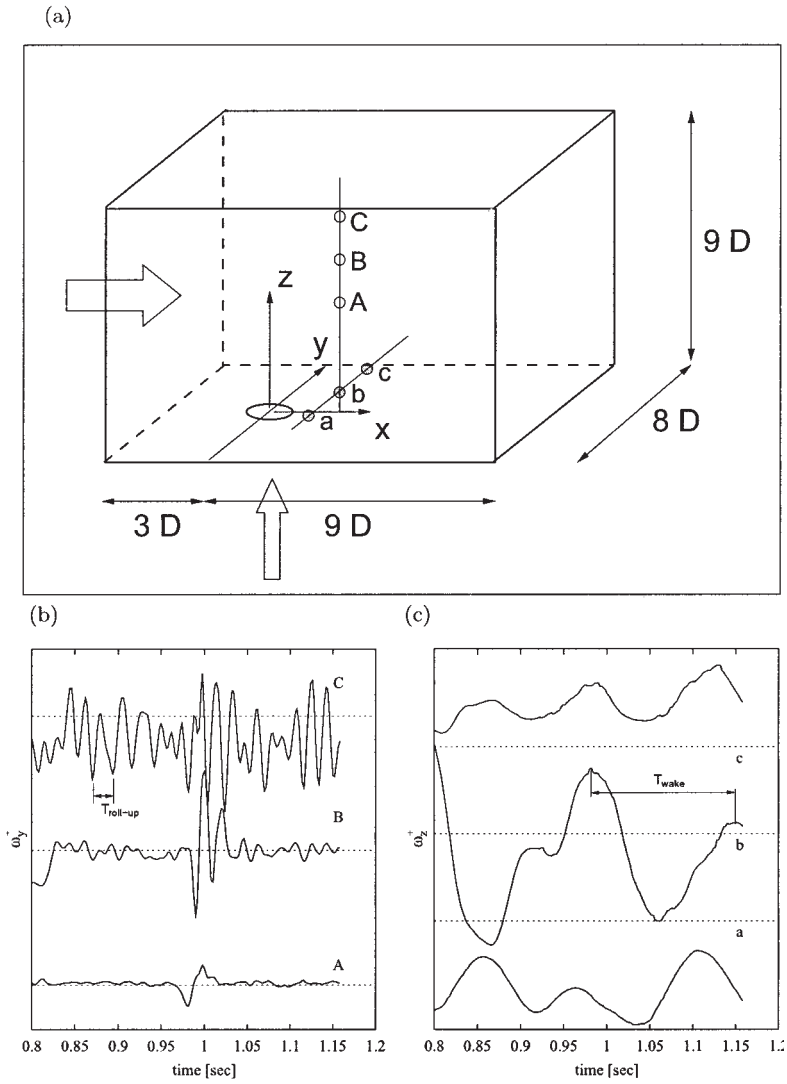

Figure 5. Characterization of large-scale flow structures.

(a) Monitoring points for evaluation of shedding frequencies (A, B, and C are at $x^+ = 2$, $y^+ = 0$, and $z^+ = 4$, 5, and 6; a, b, and c are at $x^+ = 2$, $y^+ = -0.25$, 0, 0.25, and $z^+ = 0.5$); (b) time evolution of spanwise vorticity, ω_y^+ (roll-up of shear layer vortices); (c) time evolution of wall-normal vorticity, ω_z^+ (wake vortices).

subsequent wake vortices. Signals have no noise and through autocorrelation on a time-series window corresponding to 450 time units we computed $T_{roll\text{-}up} = 0.019$ s (4.88 time units) and $T_{wake} = 0.16$ s (41.12 time units).

Following the definitions used by Moussa et al.,[39] the Strouhal numbers for wake and shear layer vortices are $S_{wake} = D/U_{cf}T_{wake} = 0.125$ and $S_{roll\text{-}up} = D/U_{cf}T_{roll\text{-}up} = 1.02$. These values are in the range observed experimentally by Moussa et al.[39] From power spectra of pressure signal, Rudman[27] calculated $S_{wake} = 0.098$ and $S_{roll\text{-}up} = 0.70-0.75$. We do not have an explanation for this discrepancy.

Particle dispersion

In the experiment by Kelso et al.[10] (Figure 1a), smoke tracers are injected in the pipe boundary layer to visualize the dynamics of the jet in the crossflow. A small fraction of tracers is captured by shear layer vortices and is advected downstream along the upper side of the jet, whereas the main fraction is entrained and accumulated in the lower side of the jet arising from the action of the counterrotating vortices, as discussed previously. In this work, inertial particles are injected in the entire cross section of the jet and we expect that shear layer vortices and counterrotating vortices will dominate their motion in the near field. We also expect that small particles will behave like smoke tracers in Figure 1a, whereas larger particle motion will be dominated by inertial forces; intermediate size particles will exhibit specific features, the object of our work.

Following the experiment by Kelso et al.,[10] we will examine first the behavior of 10-μm outer particles (that is, those released in the ring $0.47 < r^+ < 0.50$ at the pipe exit). Figure 6 shows front view (above) and top view snapshots (below) of particle positions taken at times $t^+ = 3.1$, 7.2, 11.3, and 15.4 time units after the instantaneous (that is, puff) release. In an instantaneous release, all the particles are injected in the flow at the same time and then followed along their trajectories. Consider first Figures 6a and b, taken 3.1 time units after release.

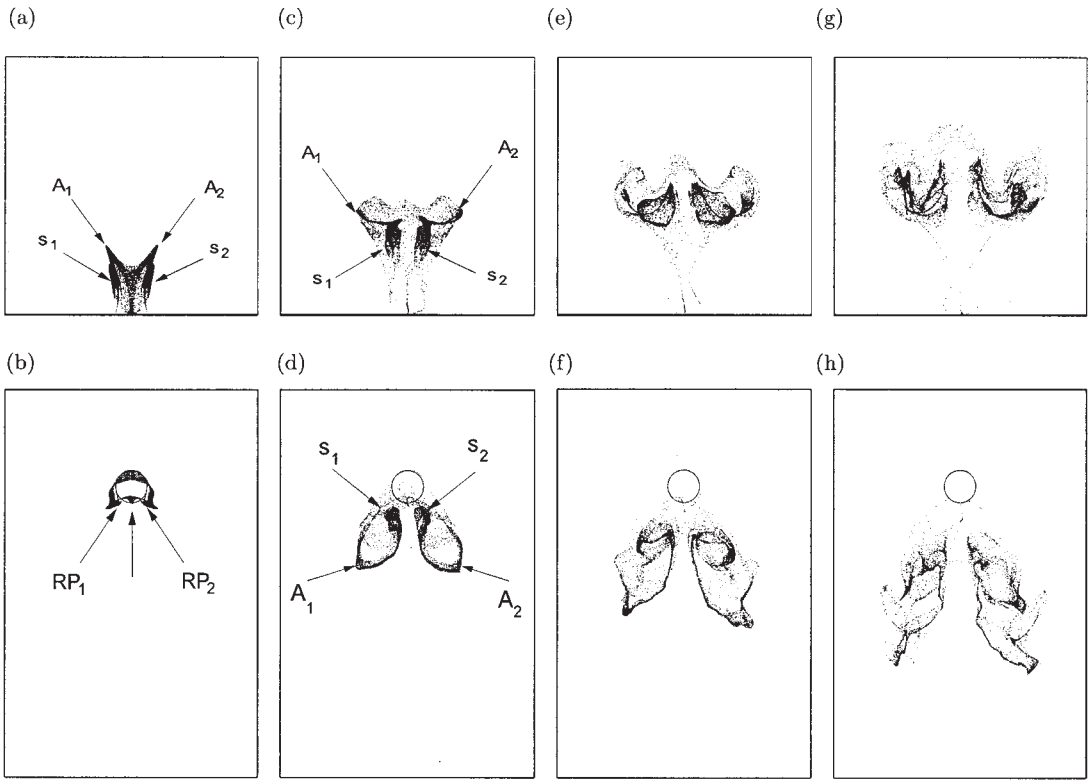

Figure 6. Front view (above) and top view (below) of 10-μm particle positions 3.1, 7.2, 11.3, and 15.4 time units after release.

Outer particles, that is, particles distributed in outer ring, $0.47 < r^+ < 0.5$ at jet exit.

Particles injected in the upstream side of the jet move along the cylindrical vortex sheet containing the jet fluid: particles are driven both downstream by the crossflow and upward by the jet. As discussed by Kelso et al. (see Figure 9 in Kelso et al.[10]), the cylindrical vortex sheet folds and rolls up at the jet sides, initiating the formation of the counterrotating vortices. Roll-up points are indicated as RP_1 and RP_2 in Figure 6b. As shown in Figure 6a, in our simulation particles coming from the upstream side of the jet accumulate into two streaks, s_1 and s_2, which align precisely where the vortex sheet folds. Particles injected from the lee side (indicated by the central arrow in Figure 6b) cluster together and move upward along the cylindrical vortex sheet, and inward toward the jet axis, thus being entrained into the jet body together with the crossflow fluid. Above the jet exit plane (roughly 1*D* above) where the jet starts to bend, clustering particles continue to move upward and bifurcate forming the two branches, A_1 and A_2.

Figures 6c and 6d show particle positions 7.2 time units after release, when particles have moved approximately 2*D* downstream and 3*D* upward. In this region, the counterrotating vortices are in the early stage of their generation process. The streaks s_1 and s_2 can still be observed from the front view (Figure 6c), whereas branches A_1 and A_2 are now nearly horizontal, deflected by the interaction with the counterrotating vortices that, in the meantime, are becoming larger. From the top view (Figure 6d), we observe that streaks s_1 and s_2 are now bent in the crossflow direction, following the reorientation of the folded cylindrical surface. As proposed by Kelso et al.,[10] the initial bending of the vortex sheet is the first sign of initiation of the counterrotating vortices and, as discussed by Cortelezzi and Karagozian,[13] enhanced mixing in the jet near field results from the *formation* of the counterrotating vortices, rather than by their *existence*. This seems to be confirmed here because we observe strong circulation in the region where the streaks form. As can be observed from the subsequent snapshots (Figures 6f and h), particles accumulated into the streaks are then dispersed by the spanwise shear layer vortices that gave birth to the streamwise counterrotating vortices.[10] From Figures 6e and g, we observe that most of the particles injected in the outer ring move along and disperse in the lower part of the jet entrained by the counterrotating vortex pair.

We turn now the attention to the behavior of inner particles, that is, those released in the inner circle at the pipe exit. Figure 7 shows front view (above) and top view snapshots (below) of particle positions taken at $t^+ = 3.1$, 7.2, 11.3, and 15.4 time units after the puff release. Consider first Figures 7a and b, showing front and top views after 3.1 time units. Particles, initially distributed uniformly in the circle, are pushed backward in the center and pulled forward along the jet sides with their distribution shaping as a crescent in the top view. In these early stages, the dispersion of inner particles appears more uniform than that of outer particles because of the absence of large velocity gradients, and thus vorticity, in the central region of the jet.

The behavior in the early stage of dispersion determines the future interaction between inner particles and flow structures of the tranverse jet. Figures 7c, 7e, and 7g clarify that the presence of particles near the jet upper boundary favors particle inter-

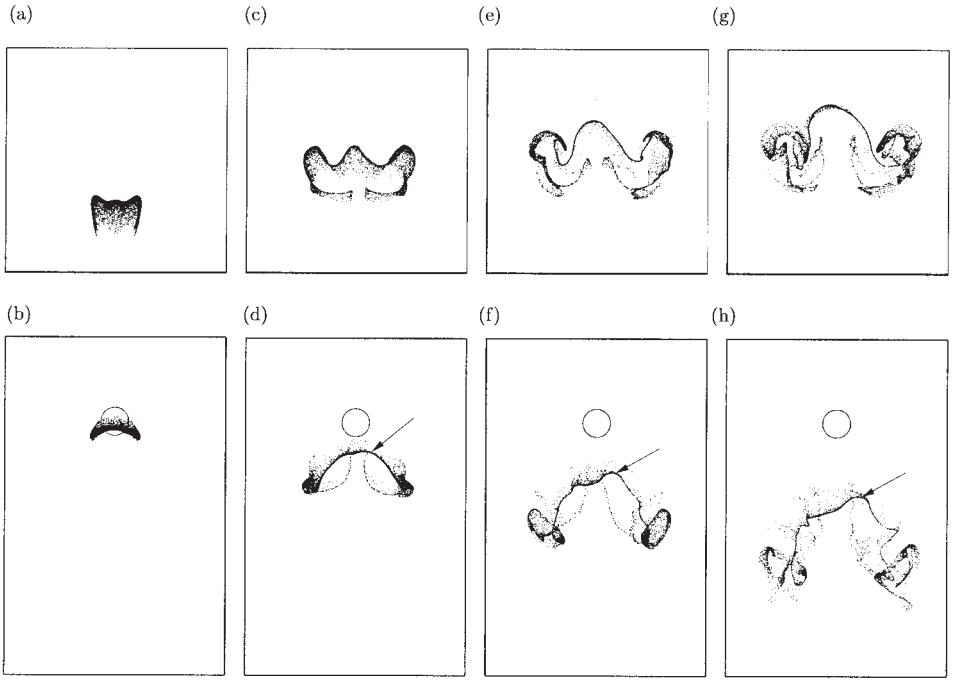

Figure 7. Front view (above) and top view (below) of 10-μm particle positions 3.1, 7.2, 11.3, and 15.4 time units after release.

Inner particles, that is, particles distributed in inner circle, $r^+ \leq 0.47$ at jet exit.

action with upper spanwise shear layer vortices, which entrain them in the upper part of the jet. From the top views in Figures 7d, 7f, and 7h, we observe that particles near the jet symmetry plane, indicated by the black arrow, move coherently in the downstream direction, aligned with the lower side of an upper spanwise shear layer vortex. We observe also that particles at the jet sides move faster in the downstream direction and are strongly dispersed by the joint action of spanwise shear layer vortices and streamwise counterrotating vortices. As shown by Figures 7e and 7g, this time particles disperse mainly in the upper part of the jet.

We will discuss now the behavior of different size particles by visualizing their position 0.112 s (that is, 28.8 time units) after puff release. In Figures 8a and 8b we show front and top views of 10-μm inner particles; in Figures 8c and 8d we show front and top views of 10-μm outer particles; in Figures 8e and f we show front and top views of 100-μm inner particles; in Figures 8g and 8h we show front and top views of 100-μm outer particles.

Figure 8a shows again the action of the shear layer vortex, which entrains a fraction of the 10-μm inner particles and drives them downstream as a single coherent filament (indicated by the black arrow). The same observation can be made examining the top view in Figure 8b. Only a small fraction of the particles is entrained by the shear layer vortex (as indicated by the arrow), and the main portion is dispersed in a larger region and in the lower part of the jet by the action of other structures, including preceding and following shear layer vortices. Turning our attention to Figures 8e and 8f, with respect to 100-μm inner particles, we can observe a rather different behavior: particles do not spread around and are advected downstream by one single structure, which is the lower side of a shear layer vortex, indicated by the arrow (we could observe this from a number of frames and animations indicating particle position *and* vorticity field).

Consider now the behavior of outer particles, shown in Figures 8c and d for the 10-μm particles and in Figures 8g and 8h for the 100-μm particles, respectively. Compared to corresponding inner particles, dispersion of outer particles occurs in larger flow regions. However, 10-μm particles show a higher nonhomogeneous distribution and appear segregated by the action of the local vortical structures.

Examination of the puff release is not as rich a source of information as examination of a continuous release, which, however, is currently not feasible in our computational laboratory. Thus, we decided to simulate a quasi-continuous release by issuing 2×10^4 particles every 0.019 s (that is, the time corresponding to $T_{roll\text{-}up}$). Figure 9, shows front and top views of the swarm at four different times, from 0.052 to 0.109 s after the release of the first group of particles. For the quasi-continuous simulation, we will show only the 10-μm outer particles because they exhibit higher dispersion. In Figures 9a and 9b we observe the evolution of the plume at the early stages of the simulation.

Figure 9a shows that particles disperse mainly in the lower part of the counterrotating vortices. From the top views in Figures 9b, 9d, 9f, and 9h, we observe that particles accumulate into regions whose shape is very similar to the Kelvin–Helmholtz billows characteristic of plane shear layers (see the arrows). At later stages (Figures 9f and 9h), the evolution of the plume becomes less coherent.

In Figure 10, the side view of inner and outer particles in the $x - z$ slab corresponding to $-0.5 < y^+ < 0.5$, superimposed to the vorticity field in the symmetry plane, will help to

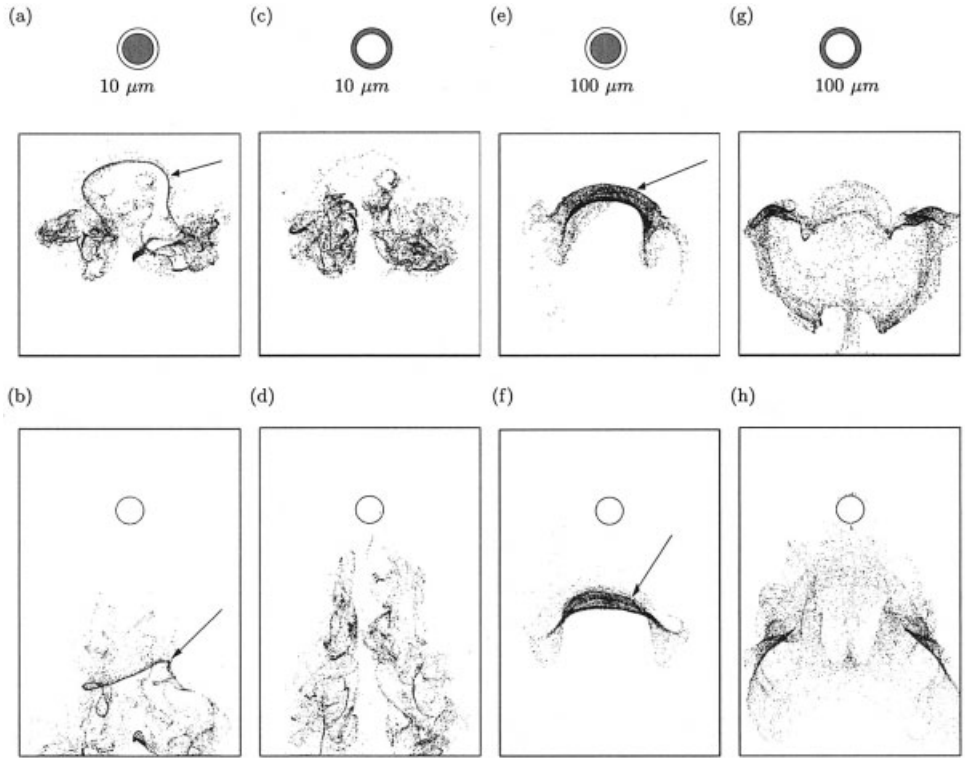

Figure 8. Particle position 0.112 s (28.8 time units) after release.

(a) and (b) Front and top view of 10-μm inner particles; (c) and (d) front and top view of 10-μm outer particles; (e) and (f) front and top view of 100-μm inner particles; (g) and (h) front and top view of 100-μm outer particles.

elucidate two main features of particle dispersion. Figure 10a shows that particles accumulate in two different regions of the jet. A small fraction of particles, indicated by arrow A, is near the jet axis (dash–dot line), between the positive and the negative closed contours of vorticity characterizing a shear layer vortex (isocontours are -0.390, -0.195, solid lines,

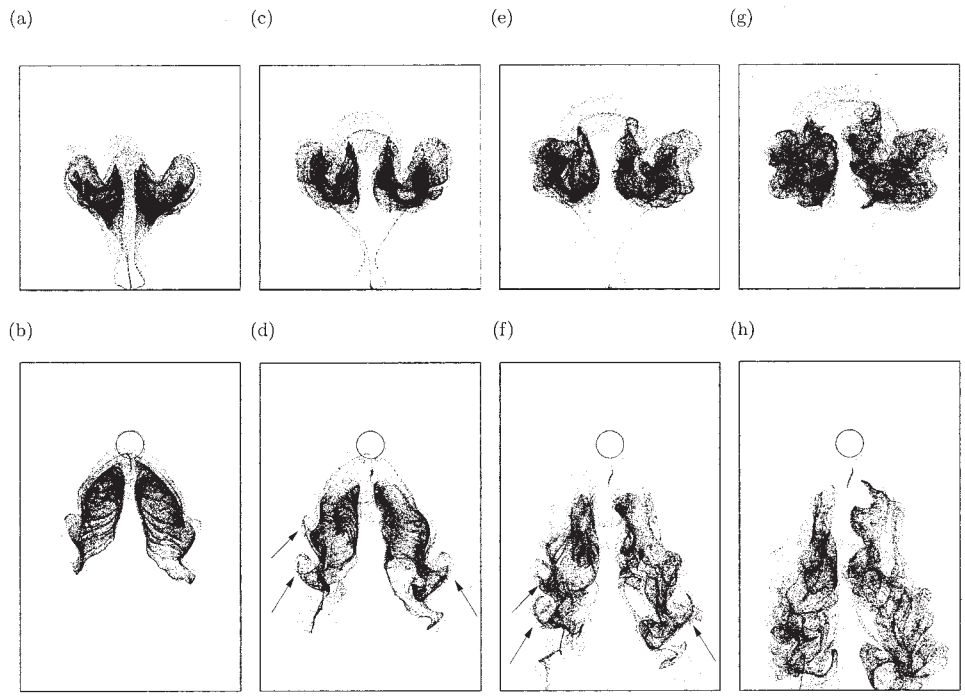

Figure 9. Time evolution of dispersion for quasi-continuous release of 10-μm outer particles.

(a) Front and (b) top view 0.052, 0.071, 0.09, and 0.109 s (13.3, 18.2, 23.1, and 28. time units) after release.

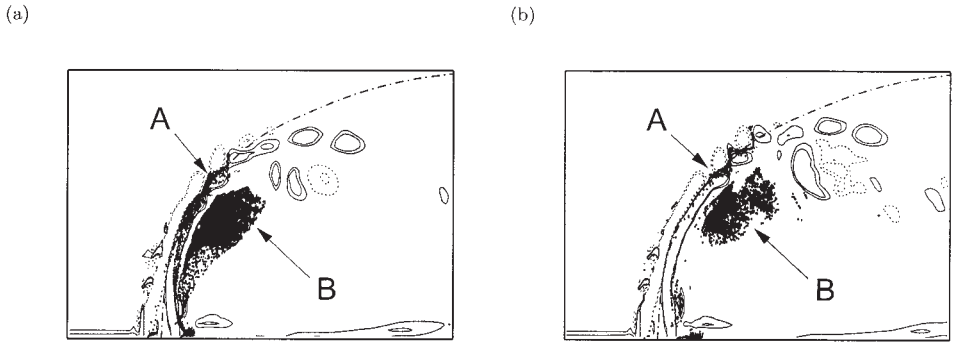

Figure 10. Preferential distribution of 10-μm particle plume under the action of shear layer vortices in jet upper side.

Particle pattern in jet symmetry plane 13.4 (a) and 18.4 (b) time units after release superimposed to spanwise vorticity isocontours. Isocontours are −0.390, −0.195 (solid lines, clockwise rotation) and 0.195, 0.390 (dashed lines, counterclockwise rotation).

clockwise rotation; and 0.195, 0.390, dashed lines, counterclockwise rotation). A larger fraction of the particles (arrow B) is in the region below the jet axis. These particles are those injected in the outer circle that are swept around the side of the jet. In Figure 10b, taken 4.88 time units later, we observe that particles in the upper part of the jet are still trapped between the shear layer vortices, which have moved downstream, and particles in the lower part of the jet left the slab exiting from the side faces as the plume moves downstream.

In Figure 11a, we show the distribution of 10-μm particles in the $y - z$ slab at $x^+ = 5 \pm 0.1$ superimposed to the dimensionless streamwise vorticity ω_x^+ (isocontours are −0.390, −0.195, dotted line and 0.195, 0.390, solid line). Particles accumulate between positive and negative vorticity isocontours. This is expected, given that rotation of vortical structures pushes particles away from the vortex core and accumulates them in the low-vorticity regions. This preferential accumulation is also apparent from Figure 11b, where particles in the $x - z$ slab at $y^+ = 1 \pm 0.1$ are superimposed to spanwise vorticity ω_y^+, and from Figure 11c where particles in the $x - y$ slab at $z^+ = 5 \pm 0.1$ are superimposed to wall normal vorticity ω_z^+ (isocontours are −0.390, −0.195, dotted lines, and 0.195, 0.390, solid lines).

We computed the correlation between particle position and the vorticity field: for all sizes, the probability density function of particle position peaks around zero values of all vorticity components.[40] Figure 11d shows the results obtained for 10-μm particles. This result was previously established from previous works, which show that particles segregate preferentially in low-vorticity regions.[8,20] We observed that 10-μm particles show the highest preferential concentration, which decreases monotonically for the others, being minimal for the 200-μm particles.

Particle segregation and dispersion

Numerical simulations discussed in this work and previous experimental observations (see Gosh and Hunt[2] and references therein) show that particles injected into a crossflow disperse differently depending on their size: small particles are driven away from the jet core and accumulated in the jet lee side, whereas larger particles may penetrate into the crossflow more than the jet and, yet, exhibit a reduced dispersion. To reproduce this complex behavior, Gosh and Hunt[2] defined four different regions in the transverse jet, and developed ad hoc models to simulate dispersion in each of these regions. The Lagrangian approach adopted in this work reproduces the observed behavior with a reduced modeling effort and helps to clarify the mechanisms responsible for differential penetration and dispersion.

Figure 12 shows the mean trajectory of the swarms of different size particles simulated in this work (symbols) and the jet axis (dotted line). Here, the mean trajectory of the spray is defined as the trajectory of the center of mass of particle swarms. The mean spray trajectory gives no explicit information on particle dispersion and segregation. Yet, because the dispersion process is controlled by the interaction between particles and fluid structures, which are found to be mostly effective in the upper side and in the lee side of the jet, the relative position of the particle swarm center of mass and the jet axis can be used to evaluate the fraction of particles that may effectively interact with the flow structures. The mean trajectory of the particle swarm lies above the jet axis for 100-, 150-, and 200-μm particles, and below the jet axis for 10- and 1-μm particles. We should remark here that particles are injected at the same velocity of the fluid, and therefore larger particles have larger momentum and penetrate deeper into the crossflow. For 100-, 150-, and 200-μm particle swarms, particle penetration is comparable with the stopping distance ($y_p^+ = v_0\tau_p/D \simeq 7$ for 100-μm particles). Because of their larger inertia, particles move into the crossflow "decoupled" from the jet flow. If the initial momentum is large enough, particles may cross the upper boundary of the transverse jet, moving away from the high shear region populated by shear layer vortices and counterrotating vortices. In the case of smaller particles ($D_p = 1$ and 10 μm), the initial momentum is not sufficient to penetrate the cross stream, and particles are close to dynamic equilibrium with the issuing jet and are thus deflected by the crossflow.

We compared the behavior of the smaller particles against the behavior of the fluid, calculating the dispersion of 2×10^4 fluid tracers injected at the jet exit. We found that the center of mass of the swarm of fluid tracers overlaps with the one calculated for 1-μm particles. Therefore, small particles cannot cross the upper boundary of the jet and remain in the region populated by the large-scale structures. As discussed previously, a small fraction of 10-μm inner particles may reach the

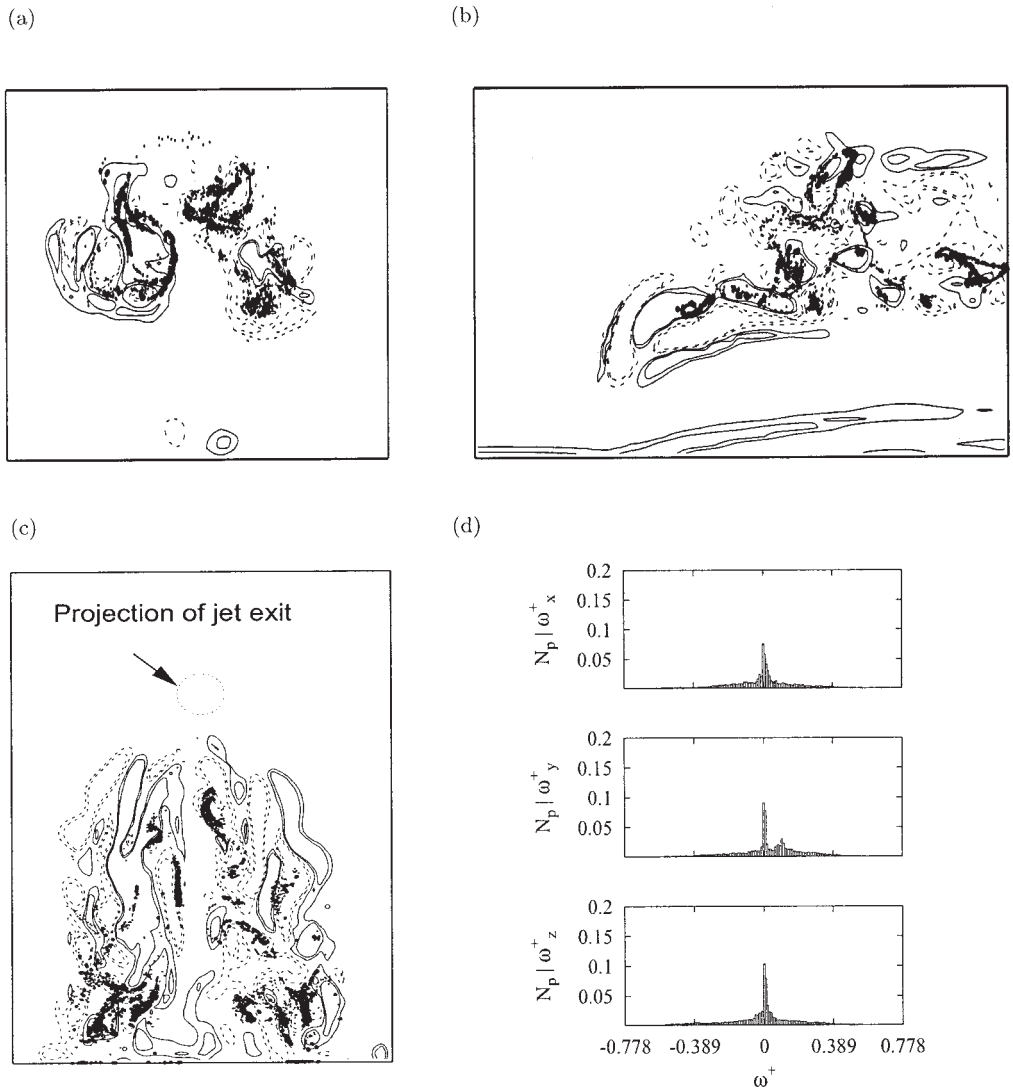

Figure 11. Preferential accumulation of 10-μm particles into low-vorticity regions.

(a) y–z plane at $x^+ = 5$, isocontours of ω_x^+ are -0.390, -0.195 (dotted line) and 0.195, 0.390 (solid line); (b) x–z plane at $y^+ = 1$, isocontours of ω_y^+ are -0.390, -0.195 (dotted line) and 0.195, 0.390 (solid line); (c) x–y plane at $z^+ = 5$, isocontours of ω_z^+ are -0.390, -0.195 (dotted line) and 0.195, 0.390 (solid line); (d) correlation between particle position and values of streamwise, spanwise, and wall normal (dimensionless) vorticities.

upper boundary of the jet and disperse in the region above the jet axis, being trapped by the upper shear layer vortices. However, the main fraction is dispersed in the lee side, under the joint action of the lower shear layer vortices and the counter-rotating vortices.

In Figure 13, the wall normal and spanwise distribution of 1-, 10-, and 100-μm particles at three transverse sections ($x/D = 2$, 5, and 8) of the computational domain are compared. To obtain statistics based on a large number of particles, we counted the number of particles crossing each transverse section during the simulated time period, and stored the y and z coordinates of particles at crossing time, y_{cr} and z_{cr}. Then, we calculated the particle number density distribution for y_{cr} and z_{cr}. These curves are shown as solid lines in Figure 13. Consider first Figure 13a, representing the distribution of 1-μm particles in the wall normal direction. The jet axis (dash–dot line) and the trajectory of the center of mass of the particle

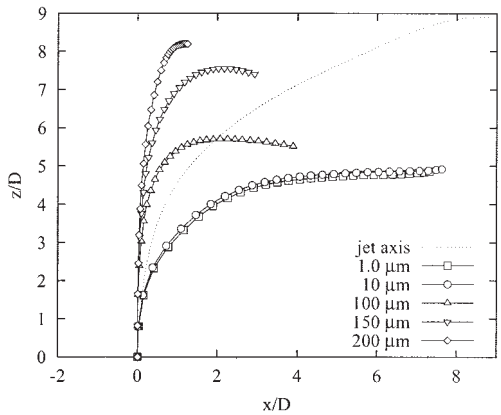

Figure 12. Jet axis (line) and trajectories of swarm center of mass for different size particles (symbols).

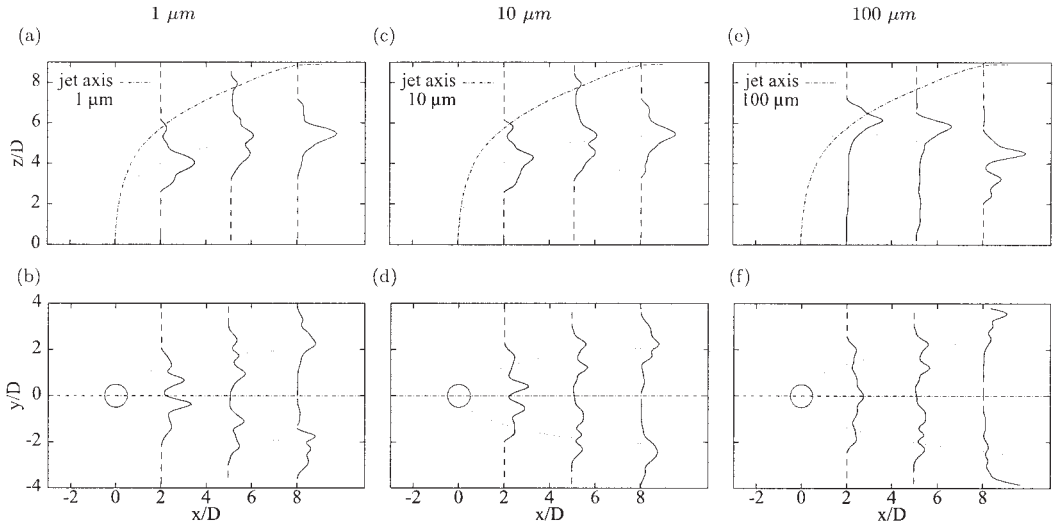

Figure 13. Jet axis (line), trajectory of swarm center of mass, and number particle distribution along wall normal and spanwise directions for different size particles (in μm): (a) 1; (b) 10; (c) 100.

swarm (dot–dot line) are also shown for reference. At $x/D = 2$ the distribution of particles in the wall normal direction peaks at the position of the center of mass of the swarm. A smaller peak is observed at the position of the jet axis. At $x/D = 5$ the wall normal distribution shows multiple peaks, with a small peak still visible at the jet axis. This peak moves out of the computational domain at $x/D = 8$, where the distribution shows again the main peak at the position of the center of mass of the swarm. Consider now Figure 13b, representing the distribution of 1-μm particles in the spanwise direction. The jet center plane (dashed line) and the mean square displacement of particles in the lateral direction (dotted line) are shown for reference. The distribution of particles in the streamwise direction is not symmetric and shows multiple peaks that move away from the jet centerplane at downstream sections. Consider now Figures 13c and 13d, representing the distribution of 10-μm particles, and Figures 13e and 13f, representing the distribution of 100-μm particles. In the wall normal direction, distributions peak at the position of the center of mass of particle swarm. For 100-μm particles, the main peak, which is above the jet axis at $x/D = 2$, moves toward the bottom wall at downstream sections. In the spanwise direction, the distribution of 100-μm particles is more uniform than that for smaller particles. Multiple peaks form at downstream sections and move away from the jet center plane. We should remark here that the asymmetry observed in the spanwise direction for particle number distribution is most likely attributable to the approach used to approximate the quasi-continuous release. The number of puffs in the sequence is not sufficient to obtain statistical stationarity of results.

Particle penetration and related dispersion effects are only one aspect of the interaction between particles and crossflow. It is also useful to define an integral parameter to characterize quantitatively the degree of particle segregation. Specifically, in different flow configurations, quasi-pure advection[41] was observed for particle timescale that was very small compared to the flow structures timescale, whereas segregation and preferential accumulation have been observed when the timescale of particles becomes comparable to that of the flow structures.[42] Here, we aim to identify the flow timescales that control the dispersion and segregation processes observed in Figures 7 and 8. To this aim, we will use the correlation dimension introduced by Grassberger and Procaccia[43] and discussed in Fessler et al.,[44] which has been used to quantify the degree of organization of particle patterns in homogeneous turbulence (see Fessler et al.[44]) and in more complex flow fields such as mixing layers and wakes.[8] The correlation dimension quantifies the (fractal) dimension of the subspace in which particles cluster. Specifically, if particles are homogeneously dispersed, the correlation dimension will be 3; if particles cluster along two dimensional surfaces, the correlation dimension will be 2, whereas if particles tend to line up, the correlation dimension will be 1. For more complex particle distributions, the correlation dimension will be a noninteger value.

Fessler et al.[44] measured the clustering of different size particles in homogeneous turbulence by examining digital photographs of particles taken in the centerline of a turbulent channel. They chose a base particle from the photo and counted the number of particles, $N(l)$, that are within a certain distance l of that base particle. Then, they defined the correlation dimension as the slope of the curve $\log[N(l)]$ vs. $\log(l/l_0)$, where l_0 is some suitably defined length scale. This process, repeated for 1000 randomly chosen base particles, was used to obtain an average value of the correlation dimension.

Tang et al.[8] extended the methodology proposed by Grassberger and Procaccia[43] to quantify particle clustering in potentially more complex flow systems. They simulated numerically the dispersion of particles injected from a restricted region in a plane mixing layer and in a wake and started computing the correlation dimension when the concurrent observation of particles and path lines indicated entrainment of injected particles by the shear flow. They calculated the correlation dimension as $\nu = \lim_{l\to 0}[1/\log(l)]\log \sum p_i^2$, where p_i is the probability that the separation distance between two particles is less than l. This procedure ensured that correlation dimension results were independent of the precise particle injection position.

We compute the correlation dimension characterizing a swarm of 10^4 particles with initial homogeneous distribution at

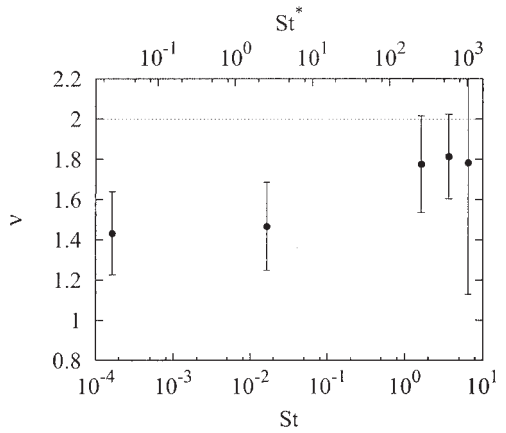

D_p [μm]	St	St^*	ν	$\pm\Delta\nu$
tracer	0	0	1.51	0.13
1.	$1.62 \cdot 10^{-4}$	$2.56 \cdot 10^{-2}$	1.43	0.21
10	$1.62 \cdot 10^{-2}$	2.56	1.47	0.22
100	1.62	$2.56 \cdot 10^{2}$	1.78	0.24
150	3.64	$5.77 \cdot 10^{2}$	1.81	0.21
200	6.47	$1.03 \cdot 10^{3}$	1.78	0.65

Figure 14. Particle correlation dimension vs. two possible scalings of Stokes number: St = $\tau_p/T_{roll\text{-}up}$ and St* = τ_p/T_{slv}.

the jet orifice. We start the computation 0.04 s (10.3 time units) after particle release, when particles start to be entrained by the large-scale structures. Similarly to Tang et al.,[8] by following this procedure the correlation dimension does not depend on particle injection position and its computation provides quantitative information about the role of flow and particle dynamics. We proceeded as follows: we chose one base particle and counted the fraction of the total number of particles $N_p(r)$ that are within a distance r from the base particle. Repeating this calculation for all possible values of r, we obtained the probability distribution of the distance between particles and the base particle. If particles are uniformly distributed in the volume surrounding the base particle, $N_p(r)$ will scale with the volume of the sphere (that is, r^3); if particles are uniformly distributed over a surface, $N_p(r)$ will scale with the area of the circle (that is, r^2), and if particles are concentrated into a line, $N_p(r)$ will scale with r. In general, particles will be distributed over complex surfaces and $N_p(r)$ will scale with r^ν, where ν is the correlation dimension: the smaller the value of ν, the more preferential the concentration.

To compute results significant from the statistical perspective, we repeated the procedure for different randomly chosen base particles and different times, averaging the results. ν was then evaluated as the slope of $N_p(r)$ vs. r in a log–log plot. Finally, we examined the correlation dimension calculated for different size particles with reference to the particle inertia parameter, made dimensionless using a relevant timescale for the flow.

From the previous discussion, particle dispersion appears dominated by the shear layer vortices: thus, the relevant flow timescale may be either $T_{roll\text{-}up}$ (that is, the frequency of formation of shear layer vortices) or T_{slv}, which is the circulation time of the shear layer vortices. $T_{roll\text{-}up}$ is the timescale used in applications of dispersion control[45] because it represents the time lag between two successive instability phenomena that promote the generation of the shear layer vortices. T_{slv} is used, for instance, by Ling et al.[46] to calculate the Stokes number in the case of particle dispersion in a mixing layer. T_{slv} scales as $\theta_{ml}/\Delta U$, where θ_{ml} is the mixing layer thickness and ΔU is the velocity difference between the two mixing streams.

We calculated the circulation time of the shear layer vortices sampling the velocity field in a Lagrangian frame of reference, moving with the vortices and we obtained $T_{slv} = 1.2 \times 10^{-4}$ s. This value scales correctly with $\theta/\Delta U$, which represents the thickness of the jet boundary layer and velocity difference between jet and crossflow at the jet exit.

In Figure 14, we show the behavior of the correlation dimension plotted against the two possible scalings for the particle characteristic time: the lower axis scales with St = $\tau_p/T_{roll\text{-}up}$ and the upper axis scales with St* = τ_p/T_{slv}. For clarity, values are also listed in Table 2. Table 2 shows also the value of ν calculated for fluid tracers, which may be used to compare particle behavior against fluid behavior. We should remark here that, because particles are injected in a restricted region of the flow, the dispersion of jet fluid tracers is limited by the rate of mixing between jet and crossflow to values lower than those expected from a homogeneous distribution.

The correlation dimension is always smaller than 2, indicating that, for all the sizes investigated, particles do not reach a uniform spatial distribution in the near field of the jet, but rather they disperse along subspaces more similar to fluid sheets. In particular, ν is minimum (at values of about 1.43 and 1.47) for the smaller particles (1 and 10 μm). This indicates that the preferential accumulation of particles mainly occurs in elongated structures, as shown in Figure 8. Interestingly, for the smaller particles the correlation dimension is slightly lower than that calculated for fluid tracers, indicating that clustering is enhanced for these specific sizes.

Our results show that a maximum of preferential accumulation of particles (that is, a minimum in the correlation dimension) exists for St smaller than 10^{-2} corresponding to St* of order one. This suggests that T_{slv} is the correct timescale for particle dispersion, which is thus dominated by the circulation of fluid in the shear layer vortices.

Table 2. Correlation Dimension ν vs. Two Possible Stokes Numbers, St = $\tau_p/T_{roll\text{-}up}$ and St* = τ_p/T_{slv}

D_p (μm)	St	St*	ν	$\pm\Delta\nu$
Tracer	0	0	1.51	0.13
1	1.62×10^{-4}	2.56×10^{-2}	1.43	0.21
10	1.62×10^{-2}	2.56	1.47	0.22
100	1.62	2.56×10^{2}	1.78	0.24
150	3.64	5.77×10^{2}	1.81	0.21
200	6.47	1.03×10^{3}	1.78	0.65

Conclusions

Dispersion of particles or droplets in a transverse stream is the result of the interaction between particles and flow structures that may lead to particle clustering and preferential accumulation. Nonuniform distribution of particles in space and time may downgrade the efficiency of process devices in a number of industrial and environmental applications.

In this work, we examined the dispersion and segregation of inertial particles injected by a jet into a transverse boundary layer, in connection with the dynamics of the large-scale structures of the flow. We used the Eulerian–Lagrangian approach to reproduce the three-dimensional, time-dependent flow field of the jet in crossflow and to simulate the behavior of large swarms of particles. We compared the dispersion patterns generated by particles released in the outer ring, $0.47 < r^+ < 0.5$, and in the inner circle, $r^+ \leq 0.47$, at the pipe exit, for 5 different orders of magnitude of the inertial parameter. We found that particles disperse differently because of the interaction with different flow structures. Comparison between spray penetration and jet penetration shows that dispersion is caused by different mechanisms, depending on particle inertia. Smaller particles are entrained by the jet and respond to the action of the structures generated by the interaction of the jet with the crossflow. Larger particles are driven by their initial inertia and rapidly cross the jet flow region: their eventual motion is thus more decoupled from the dynamics of the jet in crossflow.

The large dispersion observed for smaller particles, however, does not correspond to homogeneous particle distribution. Despite the intensive advective action of shear layer vortices and counterrotating vortices, particles line up along low vorticity regions in between vortices. A similar behavior is observed when the release of particles is quasi-continuous: 10-μm particles are modulated into subsequent fronts whose shape is very similar to the Kelvin–Helmholtz billows found in plane shear layers.

As suggested by similar analyses in different flow configurations, accumulation and segregation of particles in specific regions of the flow are observed when the flow structures timescale and the particle response time are comparable. Therefore, we tried to identify the flow timescales that control dispersion and segregation quantifying the degree of preferential concentration of particles using the correlation dimension.[43] We found the minimum of the correlation dimension, indicating maximum preferential concentration, for the smaller particles (1 and 10 μm). The characteristic time of these particles scales with the circulation time of the shear layer vortices, which are thus responsible for particle dispersion in the flow regions examined.

The analysis reported in this work represents a first step toward a deeper understanding of particle dispersion in transverse jets. We have shown that dispersion is the result of the size-dependent response of particles to large-scale flow structures originating from "natural" flow field instabilities. Large-scale flow structures are crucial for the advection of species and control the dispersion when the particle response time is comparable with the timescale characteristic of the flow. Therefore, a first way to control particle dispersion in a crossflow is to size the particles to be dispersed looking at the characteristic timescales of the flow. In turn, the characteristic timescales of the flow are a function of the jet to crossflow velocity ratio (Karagozian et al.[24] and references therein) and may change within the height of the crossflow boundary layer and with the conditions at the jet exit. Furthermore, the phasing between the time of injection of particles and the stage of development of shear layer vortices may affect particle behavior. Further analyses may include the simulation of different flow configurations (different values for the jet Reynolds number and the jet to crossflow velocity ratio) and the evaluation of the effect of the phasing between the time of injection of particles and the stage of development of shear layer vortices.

The present work shows that the extent of dispersion also depends on the position of injection point chosen for particles, which determines their probability of interaction with the large-scale, mixing enhancing structures of the flow. In our work, particles injected into the jet shear layer penetrate less and disperse more than particles injected into the core of the jet. A second way to improve dispersion in environmental and industrial devices is thus to inject particles into the high shear regions.

Finally, there is some evidence in the literature that flow structures may be modified by flow-field modulation. This introduces a third possibility for dispersion control in which the flow-field modulation is tuned to generate flow structures having a specified characteristic timescale. Promising results have been obtained in simple flow configurations (see Lazaro and Lasheras,[47] among others) and further analyses are required to extend these results to the jet in crossflow. These will be the focus of a future numerical investigation.

Acknowledgments

The authors gratefully acknowledge the help of Germana Picco in running flow and particle simulations. Thanks also to Professor Luca Cortelezzi for his insightful remarks and timely suggestions. The support of CATAS (Udine, Italy) is gratefully acknowledged. One of the authors (M.C.) is grateful to European Union for the financial support under ICOPAC Grant UE-HPRNCT-2000-00136.

Literature Cited

1. Cleaver RP, Edwards PD. Comparison of an integral model for predicting the dispersion of a turbulent jet in a crossflow with experimental data. *Journal of Loss Prevention in the Process Industries*. 1990; 3:91-96.
2. Gosh S, Hunt JCR. Spray jets in a cross-flow. *Journal of Fluid Mechanics*. 1998;365:109-136.
3. Smith SH, Mungal MG. Mixing, structure and scaling of the jet in crossflow. *Journal of Fluid Mechanics*. 1998;357:83-122.
4. Taylor GI. Diffusion by continuous movements. *Proceedings of the London Mathematical Society*. 1921;20:196-204.
5. Mungal MG, Lozano A. Some observations of a large, burning jet in crossflow. *Experiments in Fluids*. 1996;21:264-267.
6. Eaton JK, Fessler JR. Preferential concentration of particles by turbulence. *International Journal of Multiphase Flow*. 1994;20:169-209.
7. Marchioli C, Soldati A. Mechanisms for particle transfer and segregation in a turbulent boundary layer. *Journal of Fluid Mechanics*. 2002;468:283-315.
8. Tang L, Wen F, Yang Y, Crowe CT, Chung JN, Troutt TR. Self-organizing particle dispersion mechanism in a plane wake. *Physics of Fluids*. 1992;4:2244-2251.
9. Fric TF, Roshko A. Vortical structure in the wake of a transverse jet. *Journal of Fluid Mechanics*. 1994;279:1-47.
10. Kelso RM, Lim TT, Perry AE. An experimental study of round jets in a cross-flow. *Journal of Fluid Mechanics*. 1996;306:111-144.
11. Yuan LL, Street RL, Ferziger JH. Large-eddy simulations of a round jet in crossflow. *Journal of Fluid Mechanics*. 1999;379:71-104.
12. Rivero A, Ferrè JA, Giralt F. Organized motions in a jet in crossflow. *Journal of Fluid Mechanics*. 2001;444:117-149.

13. Cortelezzi L, Karagozian AR. On the formation of the counter-rotating vortex pair in transverse jets. *Journal of Fluid Mechanics*. 2001;446: 347-373.
14. Morton BR, Ibbetson A. Jets deflected in a crossflow. *Experimental Thermal and Fluid Science.* 1996;12:112-133.
15. Kelso RM, Lim TT, Perry AE. New experimental observations of vortical motions in transverse jets. *Physics of Fluids*. 1998;10:2427-2429.
16. Chung JN, Troutt TR. Simulation of particle dispersion in an axisymmetric jet. *Journal of Fluid Mechanics*. 1988;186:199-222.
17. Anderson SL, Longmire EK. Particle motion in the stagnation zone of an impinging air jet. *Journal of Fluid Mechanics*. 1995;299:333-366.
18. Apte SV, Mahesh K, Moin P, Oefelein JC. Large-eddy simulation of swirling particle-laden flows in a coaxial-jet combustor. *International Journal of Multiphase Flow*. 2003;29:1311-1331.
19. Chein R, Chung JN. Simulation of particle dispersion in a two-dimensional mixing layer. *AIChE Journal*. 1988;34:946-954.
20. Crowe CT, Chung JN, Troutt TR. Particle mixing in free shear flows. *Progress in Energy and Combustion Science*. 1989;14:171-194.
21. Wen F, Kamalu N, Chung NJ, Crowe CT, Troutt TR. Particle dispersion by vortex structures in plane mixing layers. *Journal of Fluids Engineering—Transactions of the ASME*. 1992;114:657-666.
22. Marcu B, Meiburg E. Three dimensional features of particle dispersion in a nominally plane mixing layer. *Physics of Fluids*. 1996;8:2266-2268.
23. Yang Y, Crowe CT, Chung NJ, Troutt TR. Experiments on particle dispersion in a plane wake. *International Journal of Multiphase Flow*. 2000;26:1583-1607.
24. Karagozian AR, Cortelezzi L, Soldati A, eds. *Manipulation and Control of Jets in Crossflow*. Vienna, Austria: Springer-Verlag; 2003.
25. Han KS, Chung MK. Numerical simulation of two-phase gas-particle jet in a crossflow. *Aerosol Science and Technology.* 1992;16:126-139.
26. Yi J, Plesniak MW. Dispersion of particle-laden air jet in a confined rectangular crossflow. *Powder Technology*. 2002;125:168-178.
27. Rudman M. Simulation of the near field of a jet in a cross flow. *Experimental Thermal and Fluid Science*. 1996;12:134-141.
28. Collela P, Woodward PR. The piecewise parabolic method (PPM) for gas-dynamics simulations. *Journal of Computational Physics*. 1984; 54:174-201.
29. Roe PL. Approximate Riemann solver, parameter vectors and difference schemes. *Journal of Computational Physics*. 1981;43:357-372.
30. Zang Y, Street RL, Koseff JR. A non-staggered grid, fractional step method for time-dependent incompressible Navier–Stokes equations in general curvilinear coordinate systems. *Journal of Computational Physics*. 1994;114:18-24.
31. Zang Y, Street RL. A composite multigrid method for calculating unsteady incompressible flows in geometrically complex domains. *International Journal for Numerical Methods in Fluids*. 1995;20:341-350.
32. Yule AJ. Large scale structures in the mixing layer of a round jet. *Journal of Fluid Mechanics*. 1978;89:413-432.
33. Lele SK. Compact finite differences schemes with spectral like resolution. *Journal of Computational Physics*. 1992;103:16-42.
34. Loth E. Numerical approaches for motion of dispersed particles, droplets and bubbles. *Progress in Energy and Combustion Science*. 2000; 26:161-223.
35. Maxey MR, Riley JJ. Equation of motion for a small rigid sphere in a nonuniform flow. *Physics of Fluids*. 1983;26:883-889.
36. Rowe PN, Henwood GA. Drag forces in hydraulic model of a fluidized bed—Part I. *Transactions of the Institution of Chemical Engineers*. 1962;39:43-47.
37. Hasselbrink EF, Mungal MG. Transverse jets and jet flames. Part 1. Scaling laws for strong transverse jets. *Journal of Fluid Mechanics*. 2001a;443:1-25.
38. Hasselbrink EF, Mungal MG. Transverse jets and jet flames. Part 2. Velocity and OH field imaging. *Journal of Fluid Mechanics*. 2001b; 443:27-68.
39. Moussa ZM, Trischka JW, Eskinazi S. The near field in the mixing of a round jet with a cross-stream. *Journal of Fluid Mechanics*. 1977;80: 49-80.
40. Picco G. *Analysis of the Mechanisms Controlling Inertial Particle Dispersion in Jets in Crossflow*. MS Thesis. Udine, Italy: University of Udine (in Italian); 2003.
41. Soldati A. On the effect of electrohydrodynamic flows and turbulence on aerosol transport and collection in wire-plate electrostatic precipitators. *Journal of Aerosol Science*. 2000;31:293-305.
42. Sbrizzai F, Verzicco R, Pidria M, Soldati A. Mechanisms for selective radial dispersion of microparticles in the transitional region of a confined turbulent round jet. *International Journal of Multiphase Flow.* 2004;30:1389-1417.
43. Grassberger P, Procaccia I. Measuring the strangeness of strange attractors. *Physica D*. 1983;9:189-194.
44. Fessler JR, Kulick JD, Eaton JK. Preferential concentration of heavy particles in a turbulent channel flow. *Physics of Fluids*. 1994;6:3742-3749.
45. M'Closkey RT, King JM, Cortelezzi L, Karagozian AR. The actively controlled jet in crossflow. *Journal of Fluid Mechanics*. 2002;452:325-335.
46. Ling W, Chung JN, Troutt TR, Crowe CT. Direct numerical simulation of a three dimensional temporal mixing layer with particle dispersion. *Journal of Fluid Mechanics*. 1998;358:61-85.
47. Lazaro BJ, Lasheras JC. Particle dispersion in the developing free shear layer. Part 1. The natural flow. *Journal of Fluid Mechanics*. 1992;235:143-178.

Manuscript received Oct. 20, 2003, and revision received May 21, 2004.